AIP | Physics of Fluids

Thermal stress vs. thermal transpiration: A competition in thermally driven cavity flows

Alireza Mohammadzadeh, Anirudh Singh Rana, and Henning Struchtrup

Citation: Physics of Fluids **27**, 112001 (2015); doi: 10.1063/1.4934624
View online: http://dx.doi.org/10.1063/1.4934624
View Table of Contents: http://scitation.aip.org/content/aip/journal/pof2/27/11?ver=pdfcov
Published by the AIP Publishing

PHYSICS OF FLUIDS **27**, 112001 (2015)

Thermal stress vs. thermal transpiration: A competition in thermally driven cavity flows

Alireza Mohammadzadeh,[1,a)] Anirudh Singh Rana,[2,b)] and Henning Struchtrup[1,c)]
[1]*Department of Mechanical Engineering, University of Victoria, P.O. Box 1700 Stn CSC, Victoria, British Columbia V8W 2Y2, Canada*
[2]*Aerospace Computational Modeling Laboratory, Department of Aerospace and System Engineering, Gyeongsang National University, Jinju, Gyeongnam 660-701, South Korea*

(Received 28 April 2015; accepted 8 October 2015; published online 2 November 2015)

The velocity dependent Maxwell (VDM) model for the boundary condition of a rarefied gas, recently presented by Struchtrup ["Maxwell boundary condition and velocity dependent accommodation coefficient," Phys. Fluids **25**, 112001 (2013)], provides the opportunity to control the strength of the thermal transpiration force at a wall with temperature gradient. Molecular simulations of a heated cavity with varying parameters show intricate flow patterns for weak, or inverted transpiration force. Microscopic and macroscopic transport equations for rarefied gases are solved to study the flow patterns and identify the main driving forces for the flow. It turns out that the patterns arise from a competition between thermal transpiration force at the boundary and thermal stresses in the bulk. [http://dx.doi.org/10.1063/1.4934624]

I. INTRODUCTION

The behavior of rarefied gases differs from the predictions of classical hydrodynamics in many ways.[1–5] When the Knudsen number $\mathrm{Kn} = \lambda/L$, defined as the ratio of mean free path λ and macroscopic relevant length scale L, is sufficiently small, classical hydrodynamics prevails, with well known effects such as stresses caused by velocity gradients, as expressed in the Navier-Stokes law, and heat flux caused by temperature gradients, as expressed in Fourier's law. When, however, the Knudsen number becomes larger, so-called rarefaction effects influence the flow, such as heat flux not driven by a temperature gradient, but by gradients of stresses, and *thermal stresses* caused not by velocity gradients, but by gradients of heat flux.[6–9]

Moreover, also the interaction between gas and solid boundaries depends on the degree of rarefaction. In classical hydrodynamics, one commonly assumes no-slip-no-jump boundary conditions, where the gas at the wall assumes velocity and temperature of the wall. Rarefaction leads to deviation of this behavior, so that the gas experiences velocity slip and temperature jump at the wall.[1,3,5] A particularly interesting boundary effect is *transpiration flow* (also known as thermal creep flow),[3,10–12] where velocity slip is induced by a temperature gradient in the wall, i.e., the gas is forced into motion at the boundary. Based on this effect, small amounts of gas can be moved in Knudsen pumps.[13] The interplay between the thermal stress and the thermal transpiration, and their contribution to the slip velocity has been studied using the asymptotic theory.[14–16]

A rarefied gas may be subjected to *two* different thermal forces: (a) a transpiration force due to a temperature gradient in the wall, (b) thermal stresses, due to temperature gradients in the bulk of the gas. These two forces might be acting in the same direction, hence amplifying each other, or they might be acting against each other. In the following, we will examine both cases, based on a recently

a)alirezam@uvic.ca
b)anirudh@uvic.ca
c)struchtr@uvic.ca. URL: http://www.engr.uvic.ca/~struchtr/.

presented microscopic model for wall boundary conditions that allows to control the strength and direction of transpiration flow.[17] Specifically, we shall consider a gas confined in a closed cavity with temperature gradients in the walls that induce transpiration flow and simultaneously cause a temperature profile in the bulk that induces thermal stresses. Simulations are performed with the direct simulation Monte Carlo method, which provides a microscopic solution, and with various macroscopic models, such as Navier-Stokes-Fourier equations, and the regularized 13 moment (R13) equations.

The direct simulation Monte Carlo method (DSMC) is a particle based microscopic method for solving the Boltzmann equation.[4,18,19] While it provides accurate solutions, it is numerically costly, but it does not give further insight into the observations. The DSMC method allows to determine macroscopic quantities such as temperature, velocity, stress, and heat flux, but it is, e.g., unable to distinguish between frictional and thermal contributions to stress.

Macroscopic methods derive equations directly for the macroscopic quantities, and relations between, e.g., stress and gradients of velocity and heat flux are directly present in the equations. As will be demonstrated below, this allows a deeper understanding and analysis of the observed flow patterns, i.e., between cause and effect.

Three different macroscopic models will be used for simulation and discussion: (a) the Navier-Stokes-Fourier (NSF) equations of classical hydrodynamics;[1–5] (b) equations for slow non-isothermal flow (SNIF) which add thermal stresses to NSF;[6,7,20] (c) the regularized 13 moment equations (R13) which give a further extension to hydrodynamics including coupling between temperature, velocity, stress and heat flux in the bulk, as well as a reasonable approximation to the Knudsen layers at walls.[5,21–24]

The three sets of equations can be found as approximations of the Boltzmann equation, based on suitable expansions in the Knudsen and Mach numbers. The NSF equations arise as the *first* order approximation in Kn, the SNIF equations are a reduced *second* order approximation in Kn for small Mach numbers, and the R13 equations are a full *third* order approximation in Kn for arbitrary Mach numbers.

The jump and slip boundary conditions for the macroscopic sets are derived from the boundary condition for the Boltzmann equation with the reflection kernel for velocity dependent accommodation model (VDM) presented in Ref. 17, which allows to influence the strength and direction of the transpiration force. This reflection kernel is a generalization of Maxwell's accommodation model[25] with velocity dependent accommodation coefficients. Although the Cercignani-Lampis-Lord model[26,27] improved the simplicity in the original Maxwell model, by providing two different coefficients to fit to the slip velocity and temperature jump, it does not allow to vary the strength of the transpiration force.[28] The VDM model, on the other hand, provides sufficient flexibility to be fitted to the data for thermal transpiration coefficient.

In Ref. 29, the VDM boundary condition has been incorporated in the DSMC method and was used to simulate the flow formation in a cavity with temperature gradient on the surface in the early transition regime. While using the Maxwell fully diffusive surface resulted in only two large transpiration vortices in the flow field, we observed that certain sets of coefficients in the VDM boundary conditions can lead to appearance of secondary vortices in front of the walls. However, with only a DSMC solution at hand, we could only speculate on the origin of the observed flow patterns as being an interplay between thermal stresses and transpiration forces.

In the current study, we employ the VDM model to obtain the macroscopic boundary equations for the NSF, SNIF, and R13 equations, which simplify to the conventional boundary conditions for the Maxwell model in the case of vanishing velocity dependency on the reflection kernel. Then, we use the DSMC, R13, SNIF, and NSF equations to study the flow formation inside a cavity with temperature gradient on the surface. Analysis of the results obtained from the macroscopic equations allows us to understand the flow patterns from the interplay between transpiration forces and thermal stresses. In particular, it becomes clear that for inverted transpiration force the narrow vortex in the Knudsen layer at the wall is driven by the transpiration force while the larger vortex in the bulk is driven by thermal stresses. NSF cannot describe this behavior, since it cannot account for thermal stresses, and SNIF cannot describe vortex at the wall, since it cannot describe Knudsen layer effects. The R13 equations give a good approximation to the DSMC results and allow to analyze the flow pattern as the result of the competition between thermal stresses and transpiration flow. The VDM boundary conditions

permits manipulating the strength of the thermal transpiration process, which subsequently provides a room for the thermal stresses to play a bigger role in determining the flow formation. Although the flow is in the mid-slip regime, our simulation reveals that the Knudsen layer terms are required to accurately model the DSMC results with a set of macroscopic equations.

II. MICROSCOPIC DESCRIPTION

A. Distribution function and Boltzmann equation

In kinetic theory, the state of a monatomic gas is described by the distribution function, $f(t, x_i, c_i)$, defined such that the number of particles in a phase space element $d\mathbf{x}d\mathbf{c}$ at time t is given by $f d\mathbf{x}d\mathbf{c}$, where c_k is the particle velocity, and x_i is the location in space. The Boltzmann equation relates the time evolution of the distribution function to the translation and collision of the particles in the gas as[1,2]

$$\frac{\partial f}{\partial t} + c_k \frac{\partial f}{\partial x_k} = \mathcal{S}(f, f), \tag{1}$$

where we ignored external body forces, and $\mathcal{S}(f, f)$ is the collision term.

Macroscopic properties of the gas are moments of the distribution function. In particular, mass density ρ, velocity v_i, temperature T, shear stress σ_{ij}, and heat flux q_i are given by

$$\begin{aligned} \rho = m\int f d\mathbf{c},\ \ v_i = \frac{m}{\rho}\int c_i f d\mathbf{c},\ \ 3RT = \frac{m}{\rho}\int C^2 f d\mathbf{c}, \\ \sigma_{ij} = m\int C_{\langle i} C_{j\rangle} f d\mathbf{c},\ \ 2q_i = m\int C_i C^2 f d\mathbf{c}, \end{aligned} \tag{2}$$

where the integration is performed over the velocity space $\mathbf{c}$ and m denotes the mass of a particle, R is the specific gas constant and $C_i = c_i - v_i$ is the peculiar velocity of the gas particles.

B. Boundary conditions

In order to describe the gas-surface behavior we need the distribution function at an infinitesimal neighborhood of the wall, which in the rest frame of the wall reads

$$\bar{f} = \begin{cases} f^*(c_i, x_i, t), & c_k^W n_k \geq 0 \\ f(c_i, x_i, t), & c_k^W n_k \leq 0. \end{cases} \tag{3}$$

Here, the phase density of particles leaving the wall ($c_k^W n_k \geq 0$) is expressed through the reflection kernel $\mathcal{P}$ as

$$f^* = \frac{1}{|c_n|}\int_{c_n^W<0} f\left(c_k'\right)\mathcal{P}\left(c_k' \to c_k\right)|c_n'|\, d\mathbf{c}'. \tag{4}$$

In the velocity dependent Maxwell boundary condition, the reflection kernel is a superposition of diffusive reflection, specular reflection, and isotropic scattering,[17]

$$\begin{aligned} \mathcal{P}\left(\mathbf{c}' \to \mathbf{c}\right) = \Theta\left(c'\right)\frac{|c_n|\exp\left(-\frac{mc^2}{2kT}\right)\Theta(c)}{\int\limits_{c_n>0}|c_n|\exp\left(-\frac{mc^2}{2kT}\right)\Theta(c)\, d\mathbf{c}} + \left(1-\Theta\left(c'\right)\right) \\ \left[\gamma\delta\left(c_k' - c_k + 2n_j c_j n_k\right) + (1-\gamma)\frac{1}{\pi}\frac{|c_n|}{c'^3}\delta\left(c'-c\right)\right]. \end{aligned} \tag{5}$$

Here, the particles colliding with and being reflected from the surface have the velocities c_k' and c_k, respectively. The normal component of the velocity to the surface is denoted by $c_n = c_k n_k$, and c is the absolute value of the particle velocity. The velocity dependent accommodation coefficient $\Theta\left(c'\right)$ is the probability that a colliding particle will have a thermalizing collision. Moreover, $\left(1-\Theta\left(c'\right)\right)\gamma$ is the probability that the incoming particle will be specularly reflected.

Many meaningful models for the coefficients $\Theta(c')$ and γ can be developed.[30] We follow the model suggested in Ref. 17, where $\gamma = const$ and the thermalization is assumed as a thermally activated process,

$$\Theta\left(c'\right) = \Theta_0 \exp\left(\frac{\varepsilon - \alpha\frac{m}{2}c'^2}{kT_W}\right) = \Theta_0(T_W)\exp\left(\frac{-\alpha\frac{m}{2}c'^2}{kT_W}\right). \tag{6}$$

In this relation, the strength of the activation process is denoted by the non-dimensional coefficient α. Moreover, ϵ considers the effect of energy bounce on the reflected particle, and Θ_0 is a constant depending on the wall structure. This model reduces to the original Maxwell model, when there is no activation process and no energy bounce, i.e., for $\alpha = \epsilon = 0$. The three independent coefficients in the VDM model, i.e., α, γ, and $\Theta = \Theta_0 \exp\left(\frac{\varepsilon}{kT_W}\right)$, can be used to fit to the experimental results.[17] In the current study, we set $\Theta = 1$ and explore the influence of the coefficients α and γ.

C. DSMC method

The DSMC method is a statistical particle method for the solution of the Boltzmann equation; each simulating particle represents a large number of real gas molecules.[4] Due to its statistical nature, the DSMC method requires large computational overhead, especially when the average flow velocity is small, but the results are highly accurate. We have presented an implementation of the VDM boundary conditions for DSMC in Ref. 29, where we also studied the influence of the boundary coefficients α and γ on the flow pattern in a heated cavity. The flow patterns observed and discussed there are the same as those discussed below, albeit for different Knudsen numbers. In Ref. 29, we tried to explain the observation by means of macroscopic quantities, in particular, thermal stresses, but the arguments were not conclusive. Therefore, we now proceed by solving the problem with various sets of macroscopic transport equations, which will allow us to understand the flow details better.

III. MACROSCOPIC TRANSPORT EQUATIONS

The macroscopic description of rarefied flows requires models that go beyond NSF equations of classical hydrodynamics. In recent years, we have had good success with describing rarefied flows at moderate Knudsen numbers by the R13 equations, which we will use here as well. We also will consider the NSF equations with jump and slip boundary conditions, and an extension of the latter which includes thermal stresses and is appropriate for SNIF.

All models are based on the conservation laws for mass, momentum, and energy, but use different equations for stress σ_{ij} and heat flux q_i. The conservation laws read

$$\begin{aligned} \frac{D\rho}{Dt} + \rho\frac{\partial v_k}{\partial x_k} &= 0, \\ \rho\frac{Dv_i}{Dt} + \frac{\partial p}{\partial x_i} + \frac{\partial \sigma_{ik}}{\partial x_k} &= 0, \\ \frac{3}{2}\rho\frac{D\theta}{Dt} + \left(p\,\delta_{ij} + \sigma_{ij}\right)\frac{\partial v_i}{\partial x_j} + \frac{\partial q_k}{\partial x_k} &= 0, \end{aligned} \tag{7}$$

where $\frac{D}{Dt} = \frac{\partial}{\partial t} + v_k\frac{\partial}{\partial x_k}$ is the convective derivative, $p = \rho RT = \rho\theta$ is the pressure obeying the ideal gases law, and $\theta = RT$ is the temperature in units of specific energy.

A. R13 equations

In the R13 equations, stress σ_{ij} and heat flux q_k are considered as flow variables with their own balance equations, which read for Maxwell molecules,[5,9,21,31]

$$\frac{D\sigma_{ij}}{Dt} + \underline{\underline{\frac{4}{5}\frac{\partial q_{\langle i}}{\partial x_{j\rangle}}}} + \sigma_{ij}\frac{\partial v_k}{\partial x_k} + 2\sigma_{k\langle i}\frac{\partial v_{j\rangle}}{\partial x_k} + \frac{\partial m_{ijk}}{\partial x_k} = -\frac{\rho\theta}{\mu}\underbrace{\left(2\mu\frac{\partial v_{\langle i}}{\partial x_{j\rangle}} + \sigma_{ij}\right)}, \tag{8}$$

$$\frac{Dq_i}{Dt} + \frac{5}{2}\sigma_{ik}\frac{\partial\theta}{\partial x_k} - \frac{\theta\sigma_{ik}}{\rho}\frac{\partial\rho}{\partial x_k} - \frac{\sigma_{ik}}{\rho}\frac{\partial\sigma_{kl}}{\partial x_l} + \theta\frac{\partial\sigma_{ik}}{\partial x_k} + \frac{7}{5}\left(q_k\frac{\partial v_i}{\partial x_k} + q_i\frac{\partial v_k}{\partial x_k}\right)$$
$$+ \frac{2}{5}q_k\frac{\partial v_k}{\partial x_i} + \frac{1}{6}\frac{\partial \Delta}{\partial x_i} + \frac{1}{2}\frac{\partial R_{ik}}{\partial x_k} + m_{ijk}\frac{\partial v_j}{\partial x_k} = -\frac{2}{3}\frac{\rho\theta}{\mu}\underline{\left(\frac{15}{4}\mu\frac{\partial\theta}{\partial x_i} + q_i\right)}. \quad (9)$$

Indices inside angular brackets denote the symmetric trace-free part of tensors.[5] The coefficients $(\frac{4}{5}, 1, 2, \ldots)$ are valid for the Maxwell molecules. The R13 equations for other molecule types were derived in Ref. 23, where the method is outlined and coefficients are given for hard sphere molecules. Here, we are interested in comparing the thermal stress and thermal transpiration and used the R13 equations in their most convenient form, which is for Maxwell molecules. In the equations above, $\mu = \mu_0\frac{\theta}{\theta_0}$ is the shear viscosity with μ_0 is viscosity at a reference temperature θ_0. The underlined terms in the equations will be discussed in Subsections III B and III C. Balance equations (8) and (9) contain the higher moments m_{ijk}, Δ, R_{ij} which are given by the constitutive equations[9]

$$\begin{aligned}
\Delta &= 5\frac{\sigma_{kl}\sigma_{kl}}{\rho} + \frac{56}{5}\frac{q_k q_k}{p} - 12\mu\left(\theta\frac{\partial\left(q_k/p\right)}{\partial x_k}\right),\\
R_{ij} &= \frac{20}{7}\frac{\sigma_{k\langle i}\sigma_{j\rangle k}}{\rho} + \frac{192}{75}\frac{q_{\langle i}q_{j\rangle}}{p} - \frac{24}{5}\mu\left(\theta\frac{\partial\left(q_{\langle i}/p\right)}{\partial x_{j\rangle}}\right),\\
m_{ijk} &= \frac{20}{15}\frac{q_{\langle i}\sigma_{jk\rangle}}{p} - 2\mu\left(\theta\frac{\partial\left(\sigma_{\langle ij}/p\right)}{\partial x_{k\rangle}}\right).
\end{aligned} \quad (10)$$

The R13 equations are an extension of the well-known 13 moment equations of Grad,[32] where these higher order moments vanish, $R_{ij} = m_{ijk} = \Delta = 0$. These higher order terms are obtained by the regularization technique in the R13 set, and the analysis of the R13 equations shows that these contributions are directly linked to the occurrence of Knudsen layers. By means of the Chapman-Enskog expansion, it can be shown that the R13 equations are of third order accuracy in terms of the Knudsen number.[5,21] We point out that over the years our work produced subtle changes in the above constitutive equations; the form presented above was derived in Ref. 9 based on the requirement that the full non-linear and linearized forms of the R13 equations require the same set of boundary equations.

B. SNIF equations

The equations for slow non-isothermal flow can be obtained from a reduction of the R13 equations which considers Knudsen number and Mach number as scaling parameters. This scaling is appropriate for small velocity with rather large temperature gradients,[7] where the Knudsen number has the same order as the Mach number.[20] After the scaling, only the single and double underlined terms in R13 equations (8) and (9) remain, so that stress and heat flux are given by[20]

$$\sigma_{ij} = -2\mu\frac{\partial v_{\langle i}}{\partial x_{j\rangle}} - \frac{4}{5}\frac{\mu}{p}\frac{\partial q_{\langle i}}{\partial x_{j\rangle}} = -2\mu\frac{\partial v_{\langle i}}{\partial x_{j\rangle}} + \frac{3\mu^2}{p}\left[\frac{\partial^2\theta}{\partial x_{\langle i}\partial x_{j\rangle}} + \frac{1}{\theta}\frac{\partial\theta}{\partial x_{\langle i}}\frac{\partial\theta}{\partial x_{j\rangle}}\right], \quad (11)$$

$$q_i = -\frac{15}{4}\mu\frac{\partial\theta}{\partial x_i}. \quad (12)$$

Here, heat flux (12) is given by Fourier's law, while the stress differs from NSF. The first term in the right hand side of Eq. (11) is the viscous stress, i.e., the Navier-Stokes relation, and the second term describes the thermal stress.

C. NSF equations

For the laws of classical hydrodynamics, only first order terms in the Knudsen number are considered, while the Mach number is not restricted.[2,5] In this scaling, the thermal stresses are not considered, and stress and heat flux are given by the single-underlined terms in (8) and (9), i.e., the Navier-Stokes relation and Fourier's law,

$$\sigma_{ij} = -2\mu\frac{\partial v_{\langle i}}{\partial x_{j\rangle}}, \quad q_i = -\frac{15}{4}\mu\frac{\partial\theta}{\partial x_i}. \quad (13)$$

D. Macroscopic boundary conditions

For the solution of boundary value problems with the macroscopic models (R13, SNIF, NSF), we require macroscopic boundary conditions that must be derived from the microscopic boundary condition, Eq. (3). For this we follow the method outlined in Refs. 24 and 32. Considering the continuity of the normal flux of a microscopic property Ψ_A over an infinitesimal surface element δA, gives (as seen from the rest frame of the wall)

$$m \int \Psi_A c_k n_k \, f \, d\mathbf{c} \delta A = m \int \Psi_A c_k n_k \, \bar{f} \, d\mathbf{c} \delta A, \tag{14}$$

where Ψ_A are suitable polynomials of the particle velocity, c_i. Performing the integration in the above equation provides a relation between the wall properties (θ_W, v_i^W) and the moments in the gas that serve as the boundary conditions for moments.

The integration in Eq. (14) requires an expression of the distribution function f in terms of the variables, which for the R13 system is a Grad-type distribution of the form[5]

$$f_{R13} = f_M(1 + \Phi). \tag{15}$$

Here, $f_M = \frac{\rho/m}{\sqrt{2\pi\theta}^3} \exp\left[-\frac{C^2}{2\theta}\right]$ denotes the local Maxwellian, and

$$\Phi = \left(\frac{1}{8} - \frac{C^2}{12\theta} + \frac{C^4}{120\theta^2}\right)\frac{\Delta}{\rho\theta^2} + \frac{C_{\langle i}C_{j\rangle}}{2\rho\theta^2}\sigma_{ij} - \frac{1}{\rho\theta^2}\left(1 - \frac{C^2}{5\theta}\right)C_j q_j + \frac{C_{\langle i}C_j C_{k\rangle}}{6\rho\theta^3} m_{ijk} - \frac{1}{4\rho\theta^3}\left(1 - \frac{C^2}{7\theta}\right)C_{\langle i}C_{j\rangle}R_{ij}.$$

Note that in the rest frame of the wall the peculiar velocities are given by $C_k = c_k - \mathcal{V}_i$, where $\mathcal{V}_i = v_k - v_k^W$ is the slip velocity.

The appropriate velocity functions Ψ_A in Eq. (14) are chosen based on Grad's observation[32] that meaningful boundary conditions are obtained when the velocity function Ψ_A is even in the normal component of the particle velocity $c_k n_k$. The appropriate functions for the R13 equations are, for a wall with the normal in the y-direction,[24]

$$\Psi_A = \left\{1, C_x, C^2, C_y C_y, C_x C_x, C^2 C_x\right\}. \tag{16}$$

1. R13 boundary equations

Using Eq. (15) for the distribution function and performing the integration in Eq. (14) for the corresponding VDM distribution function leads to a complete set of jump and slip boundary conditions for the R13 equations. The dependence of wall kernel (5) on velocity leads to a coupling of boundary conditions. For instance, the two boundary conditions for $\Psi_A c_n = C_x c_y$ and $\Psi_A c_n = C^2 C_x c_y$ both contain the shear stress σ_{xy} and the higher moment R_{xy}. In order to have unique boundary conditions for σ_{xy} also for the reduced models, we de-coupled the two conditions such that we have separate boundary conditions for σ_{xy} and R_{xy}. In the same manner, we had to de-couple the boundary conditions for q_y and m_{yyy}. After decoupling, the boundary conditions can be written as (with $\mathcal{T} = \theta - \theta_w$)

$$\begin{aligned}
\mathcal{V}_y &= 0,\\
\sigma_{xy} &= \sqrt{\frac{2}{\pi\theta}}\left(-\lambda_{(1,1)} p \mathcal{V}_x - \frac{1}{5}\lambda_{(1,2)} q_x - \frac{1}{2}\lambda_{(1,3)} m_{xyy}\right) n_y,\\
q_y &= \sqrt{\frac{2}{\pi\theta}}\left(-\lambda_{(2,1)}\left(2p\mathcal{T} + \frac{1}{2}\theta\sigma_{yy}\right) - \frac{1}{15}\lambda_{(2,2)}\Delta - \frac{5}{28}\lambda_{(2,3)} R_{yy}\right) n_y,\\
R_{xy} &= \sqrt{\frac{2}{\pi\theta}}\left(\lambda_{(3,1)} p\theta \mathcal{V}_x - \frac{11}{5}\lambda_{(3,2)}\theta q_x - \frac{1}{2}\lambda_{(3,3)}\theta m_{xyy}\right) n_y,\\
m_{xxy} &= \sqrt{\frac{2}{\pi\theta}}\left(-\frac{1}{14}\hat{\lambda}_{(4,1)} R_{xx} - \frac{1}{14}\lambda_{(4,2)} R_{yy} - \lambda_{(4,3)}\theta\sigma_{xx} + \frac{1}{5}\lambda_{(4,4)}\theta\sigma_{yy}\right.\\
&\quad \left. - \frac{1}{5}\lambda_{(4,5)} p\mathcal{T} - \frac{1}{150}\lambda_{(4,6)}\Delta\right) n_y,
\end{aligned} \tag{17}$$

$$m_{yyy} = \sqrt{\frac{2}{\pi\theta}}\left(\frac{2}{5}\lambda_{(5,1)}p\mathcal{T} - \frac{7}{5}\lambda_{(5,2)}\theta\sigma_{yy} + \frac{1}{75}\lambda_{(5,3)}\Delta - \frac{1}{14}\lambda_{(5,4)}R_{yy}\right)n_y.$$

The above boundary conditions are linearized in the non-equilibrium quantities $\{\mathcal{V}_x, \mathcal{T}, \sigma_{ij}, q_i, \Delta, R_{ij}, m_{ijk}\}$. This assumption can lead to a small deviation from the DSMC results, when modeling strong non-equilibrium in the Knudsen layer. The nonlinear form of the boundary condition, due to the dependency of the reflection kernel on the particle velocity becomes very complicated and is not discussed in here. The coefficients $\lambda_{(i,j)}$ depend on the details of the wall collision kernel. For the standard Maxwell model, where $\alpha = \epsilon = 0$ and $\Theta = const$ is the accommodation coefficient, we have $\lambda_{(i,j)} = \frac{\Theta}{2-\Theta}$ and $\hat{\lambda}_{(4,1)} = 0$; this agrees with the boundary conditions for the R13 equations given in Refs. 24 and 31.

In Ref. 17, boundary conditions for NSF were determined from the VDM model and a reduced distribution function, for which $\Delta = R_{ij} = m_{ijk} = 0$. While the boundary conditions for σ_{xy} and q_y in Ref. 17 have the same form as above, the corresponding coefficients differ slightly from those computed here, since the coupling to other boundary conditions (for R_{xy} or m_{yyy}) was not included.

The expressions for the $\lambda_{(i,j)}$ as functions of the parameters α and γ are tedious, and their details are not presented. Instead, we show the variations of the corresponding coefficients for the boundary conditions of shear stress and heat flux, which describe velocity slip and temperature jump.

The first row of Fig. 1 shows the coefficients $\lambda_{(1,1)}, \lambda_{(1,2)}$, and $\lambda_{(1,3)}$ that determine slip effects. The strength and direction of thermal transpiration flow are determined by the ratio $\lambda_{(1,2)}/\lambda_{(1,1)}$, which for the classical Maxwell model is always positive. For the VDM model, however, for certain values of α and γ this ratio can become rather small, or even negative, such indicating that the transpiration force can be small, or even inverted. This possibility was already pointed out in Ref. 17.

The second row of Fig. 1 shows the coefficients for the normal heat flux boundary condition, $\lambda_{(2,1)}, \lambda_{(2,2)}$, and $\lambda_{(2,3)}$, which depend only on α, but not on γ, since for both, specular reflection and isotropic scattering, the energy transfer remains zero.

2. SNIF/NSF boundary conditions

For the SNIF and NSF equations, only the boundary conditions for normal velocity, shear stress and normal heat flux are required, which are obtained from Eq. (17) by removing all contributions of higher moments, so that

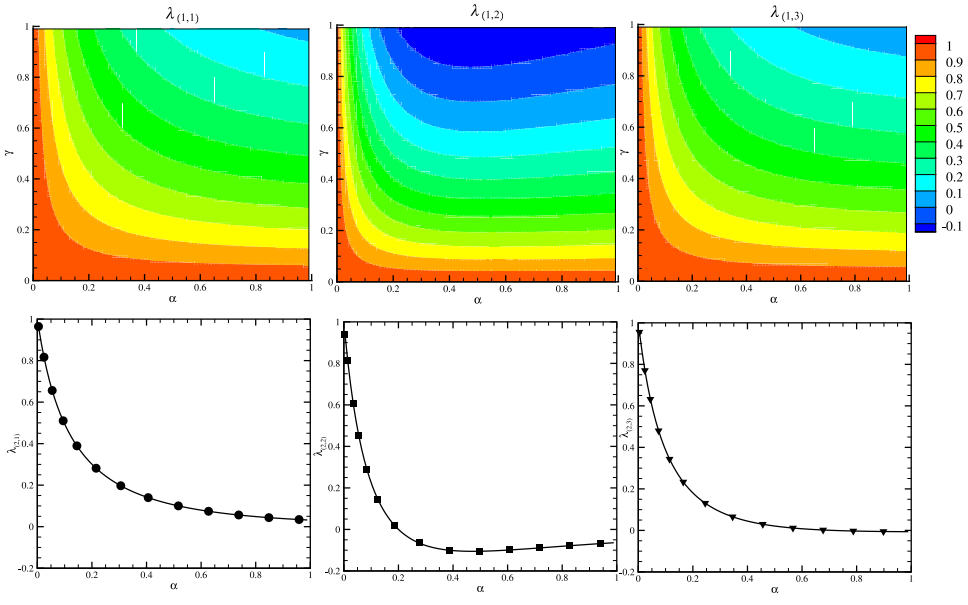

FIG. 1. Variation of the VDM coefficients $\lambda_{(i,j)}$ in boundary conditions (17). First row: coefficients for shear stress as functions of α and γ; second row: coefficients for heat flux as functions of α.

$$\begin{aligned}
\mathcal{V}_y &= 0, \\
\sigma_{xy} &= \sqrt{\frac{2}{\pi\theta}}\left(-\lambda_{(1,1)}p\mathcal{V}_x - \frac{1}{5}\lambda_{(1,2)}q_x\right)n_y, \\
q_y &= \sqrt{\frac{2}{\pi\theta}}\left(-2\lambda_{(2,1)}p\mathcal{T} - \frac{1}{2}\lambda_{(2,1)}\theta\sigma_{yy}\right)n_y.
\end{aligned} \tag{18}$$

Note that the coefficients $\lambda_{(i,j)}$ are the same as above, which implies the possibility of inverted transpiration flow also for the SNIF and NSF equations.

IV. RESULTS AND DISCUSSION

A. Geometry and methods of solution

In the current study, we consider a square micro-cavity as depicted in Fig. 2. We are interested to study the interplay between thermal transpiration and thermal stress. We consider a problem that is governed by temperature effects, with no mechanical driving forces. For this means we consider a cavity with fixed temperatures at bottom and top, and linear variation of the temperature along the side walls,

$$T_B = 600\ \text{K}, \quad T_T = 300\ \text{K}, \quad T_L(y) = T_R(y) = T_B\left(1 + \frac{y}{L}\right).$$

All boundaries of the cavity are at rest, so that the temperature gradients along the wall and inside the flow field are the sole driving forces for the rarefied flow field.

For all simulations, we consider argon ($R = 208\frac{\text{J}}{\text{kgK}}$) as Maxwell molecules with an initial equilibrium state at $T_0 = 273$ K, $\mu_0 = 1.955 \times 10^{-5}$ Pa s in a quadratic cavity of side length $L = 1$ μm. The initial density ρ_0 is set such that the initial Knudsen number is $\text{Kn}_0 = \frac{\mu_0}{\rho_0\sqrt{\theta_0}L} = 0.04$; for an average temperature $\bar{T} = \frac{1}{2}(T_B + T_T) = 450$ K this corresponds to the Knudsen number $\text{Kn} = \text{Kn}_0\sqrt{\frac{\bar{T}}{T_0}} = 0.051$. These values are sufficiently small so that one will expect good results from all three macroscopic models.

We solve the R13, SNIF, and NSF equations with the method presented in Ref. 9 and use the DSMC code discussed in Ref. 29.

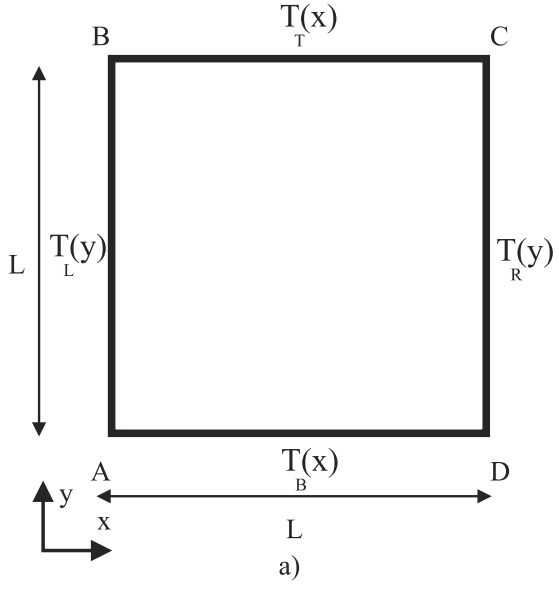

FIG. 2. Geometry and prescribed wall temperatures for the cavity.

B. Standard thermalizing surface (thermal transpiration flow)

First, we consider the standard Maxwell surface for which $\alpha = 0, \Theta_0 = 1$. With these parameters, we have the coefficients $\lambda_{(1,1)} = \lambda_{(1,2)} = 1$; hence, their ratio $\lambda_{(1,2)}/\lambda_{(1,1)} = 1$ is positive, and we expect standard transpiration force at the wall.

Thermal transpiration is a boundary effect that occurs when gas particles coming from warmer and colder regions of the flow hit the wall at the same surface element. Particles coming from the warmer region are faster and thus induce larger tangential forces on the surface compared to particles from the colder region, which are slower. As a reaction, the wall is pushed towards the colder region, or, when the wall is at rest, the rarefied gas is driven from cold to warm, which is observed here.

We compare the exact solution from DSMC with solutions for the macroscopic models in Fig. 3, which shows the velocity streamlines overlaid on the temperature distribution inside the cavity with fully diffusive surface. Microscopic and macroscopic methods exhibit two primary vortices in the flow field which push the flow from cold to warm at the side walls.

Microscopic method and the three macroscopic methods give rather similar temperature profiles in the cavity. We note that the temperature profiles only have small curvature, which implies that the thermal stresses, as expressed by the term $\frac{4}{5}\frac{\partial q_{\langle i}}{\partial x_{j\rangle}}$ in R13, Eq. (8) and in SNIF, Eq. (11), will be relatively small. Hence, in this case, the thermal stresses play only a minor role, and thus NSF, which cannot describe thermal stresses, gives rather similar results for the flow fields.

A detailed look into the temperature lines in Fig. 3 shows an almost symmetrical distribution with respect to the horizontal centerline. Considering that we have a flow in the vertical direction, one would expect that the isothermal lines be influenced by the direction of the flow, and stray away from the symmetrical distribution. However, the small values of velocity (small convection effect),

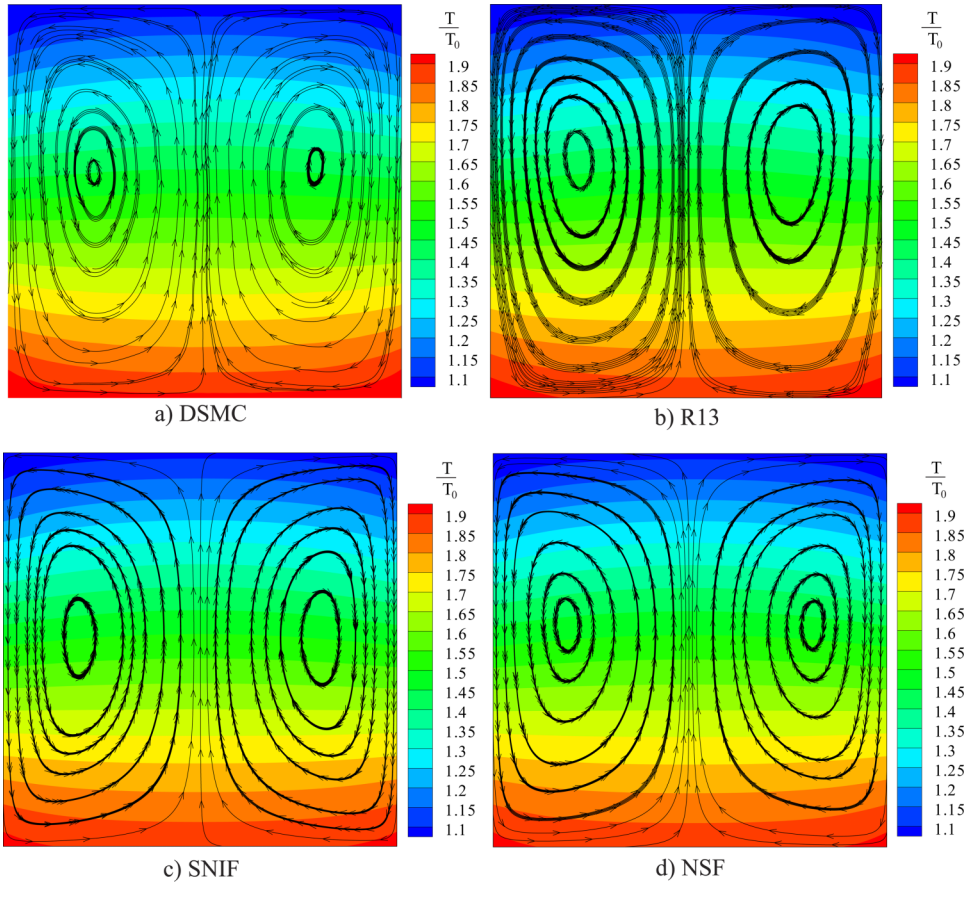

FIG. 3. Velocity streamlines overlaid on the temperature distribution for fully diffusive surface: $\alpha = 0, \Theta_0 = 1$ at $\mathrm{Kn}_0 = 0.04$.

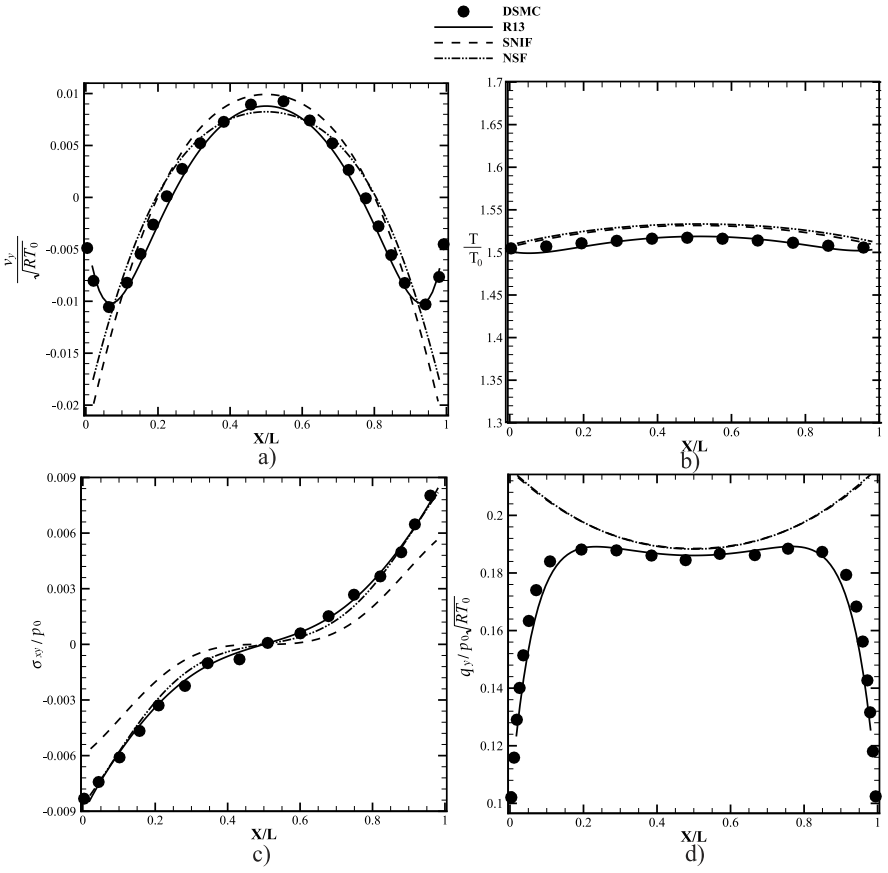

FIG. 4. Rarefied flow properties along horizontal centerline of the cavity for fully diffusive surface, $\alpha = 0$, $\Theta_0 = 1$ at $\mathrm{Kn}_0 = 0.04$. (a) Vertical velocity, (b) temperature, (c) shear stress, (d) vertical heat flux.

in comparison to the large value of temperature ratio (large conduction effect), cause the temperature lines not be significantly influenced. As a result we can observe that isothermal lines are rather symmetrical in the domain.

Figure 4 compares the flow properties along the horizontal centerline of the cavity, i.e., at $\frac{y}{L} = 0.5$. Figure 4 shows that the three macroscopic methods predict the flow velocity in the bulk of the gas, in the interval $\frac{x}{L} \in [0.1, 0.9]$, in good agreement to the DSMC simulation. However, in the proximity of the wall, i.e., in the Knudsen layer, only the R13 equations capture the wall vortex velocity. It is the presence of the Knudsen layer terms, R_{ij}, m_{ijk}, and Δ, in the R13 equations that lead to a better agreement with the DSMC solution in the proximity of the surface.

Figure 4(b) shows that the NSF and SNIF equations slightly overpredict the temperature of the gas. Moreover, the small increase in the temperature inside the Knudsen layer is only captured by the R13 equations. The variation of shear stress along the centerline is depicted in Fig. 4(c). The difference in the predicted shear stress by the SNIF equations, and the agreement between the NSF results and the DSMC data, implies the main role of the viscous stresses in the case of cavity with the Maxwell surface, while thermal stresses are slightly overemphasized in SNIF. The agreement between the R13 and DSMC in predicting normal heat flux, particularly in the Knudsen layer, is shown in Fig. 4(d).

C. Surface with inverted transpiration force

1. Thermal transpiration-thermal stress flow

Next, we employ the VDM boundary conditions and consider $\alpha = 0.2$, $\gamma = 0.9$, and $\Theta_0 = 1$. With these parameters, we have the coefficients $\lambda_{(1,1)} = 0.4613$ and $\lambda_{(1,2)} = -0.0294$; hence, their ratio $\lambda_{(1,2)}/\lambda_{(1,1)} = -0.0637$ is negative, and we expect inverted transpiration force at the wall. Note that

this ratio also reflects the strength of the transpiration force, which therefore has far smaller magnitude here than in the previous case, where it is 16 times larger.

Inverted transpiration flow occurs when most of the faster gas particles coming from the warmer region are specularly reflected, so that they do not exchange tangential momentum with the surface, while most of the slower particles coming form the colder region are thermalized or isotropically scattered and hence transmit momentum to the surface. As a reaction, the wall is pushed towards the warmer region, or, when the wall is at rest, the rarefied gas is driven from warm to cold.[29] While it is unlikely that this behavior can be found in existing materials, it can be properly modeled and analyzed in the realm of kinetic theory. For us, it provides an interesting configuration that highlights the strength and weaknesses of the models under consideration.

Figure 5 shows the velocity streamlines overlaid on the temperature distribution for this case. The DSMC method (Fig. 5(a)) predicts two sets of counter rotating vortices: Two primary vortices that drive the flow from cold to warm in the bulk of the flow, and two small vortices in the Knudsen layers that rotate from warm to cold. The temperature contours show more curvature than before, so that thermal stress contributions can be expected to play a more prominent role.

We now use the macroscopic models to interpret the DSMC result. The R13 equations (Fig. 5(b)) predict the same set of vortices as DSMC and show good agreement with the DSMC results. The SNIF (Fig. 5(c)) and NSF (Fig. 5(d)) equations, however, both fail to predict these vortices in the flow field, with the SNIF result showing only two cold-to-warm (primary) vortices, and NSF predicting only two warm-to-cold (secondary) vortices.

The NSF equations do not account for thermal stresses, so that the only driving force for the flow is the—inverted (and small)!—transpiration force at the wall. Accordingly, the NSF equations predict the inversion of the thermal transpiration to drive the flow from warm to cold.

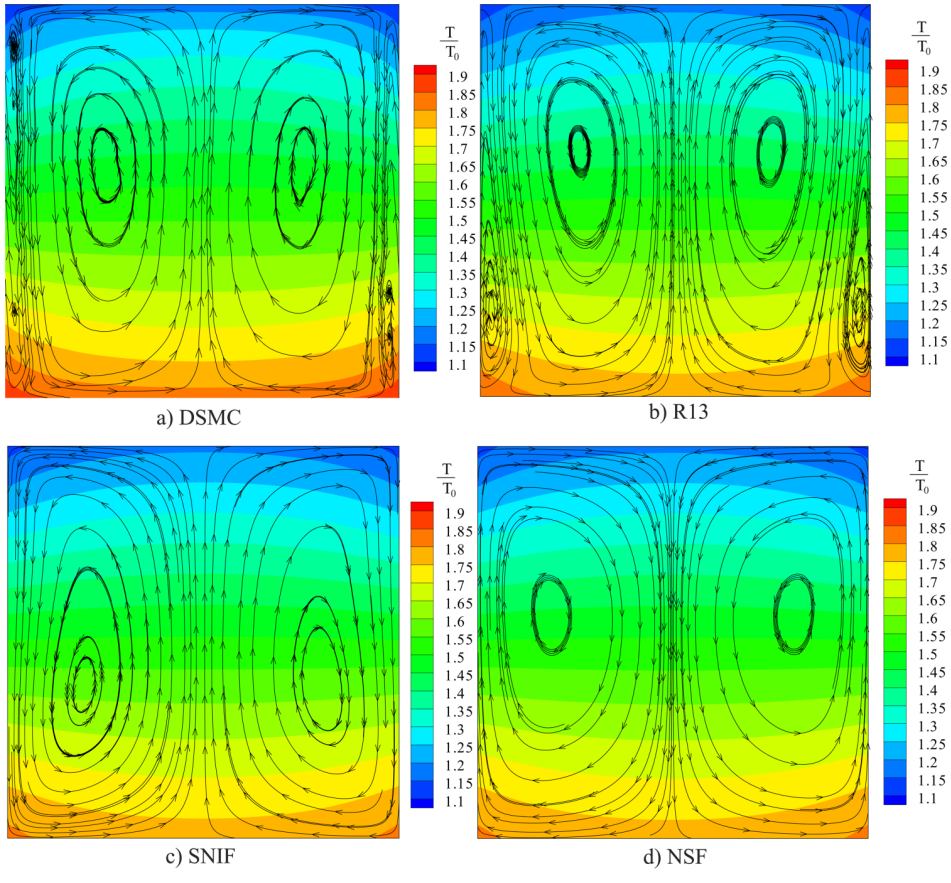

FIG. 5. Velocity streamlines overlaid on the temperature distribution for the VDM boundary conditions, $\alpha = 0.2$, $\gamma = 0.9$, and $\Theta_0 = 1$ at $\mathrm{Kn}_0 = 0.04$.

The SNIF equations, on the other hand, account for thermal stress in the bulk, as well as for the—small (and inverted)!—transpiration force at the wall. While the transpiration force tries to push the gas at the wall from warm to cold, the thermal stresses push in the opposite direction. Since the ratio $\lambda_{(1,2)}/\lambda_{(1,1)}$ is rather small, the transpiration force is weak, and the thermal stresses prevail, so that the gas at the wall moves from cold to warm.

The R13 equations describe a larger number of rarefactions effects, in particular, they reasonably reproduce Knudsen layers at the wall. With this, they can reproduce the behavior of the gas as predicted by the DSMC simulation.

Comparing all models, the following picture emerges: the observed flow pattern is the result of competition between the thermal transpiration at the boundary and the thermal stresses in the bulk, which are both due to the thermal profile induced by the wall temperatures. In the presence of the standard Maxwell boundary condition, the thermal transpiration at the wall amplifies the thermal stress in the bulk and drive the flow from cold-to-warm. That leads to appearance of two large vortices as in Fig. 3. These vortices are mainly induced by the thermal transpiration force (first order effect in Knudsen number) and can be captured by all the macroscopic methods.

However, if we change the magnitude and direction of the thermal transpiration force at the boundary, so that it acts against the thermal stress, we can, more clearly, observe the interplay between these two forces. Figure 5 shows the weak inverted transpiration force at the boundary that can only move a small amount of the gas close to the wall. This force does not suffice to overcome the thermal stresses in the bulk; as a result we observe two types of vortices in this problem. A narrow transpiration driven vortex at the wall, and the wider thermal stress driven vortex in the bulk.

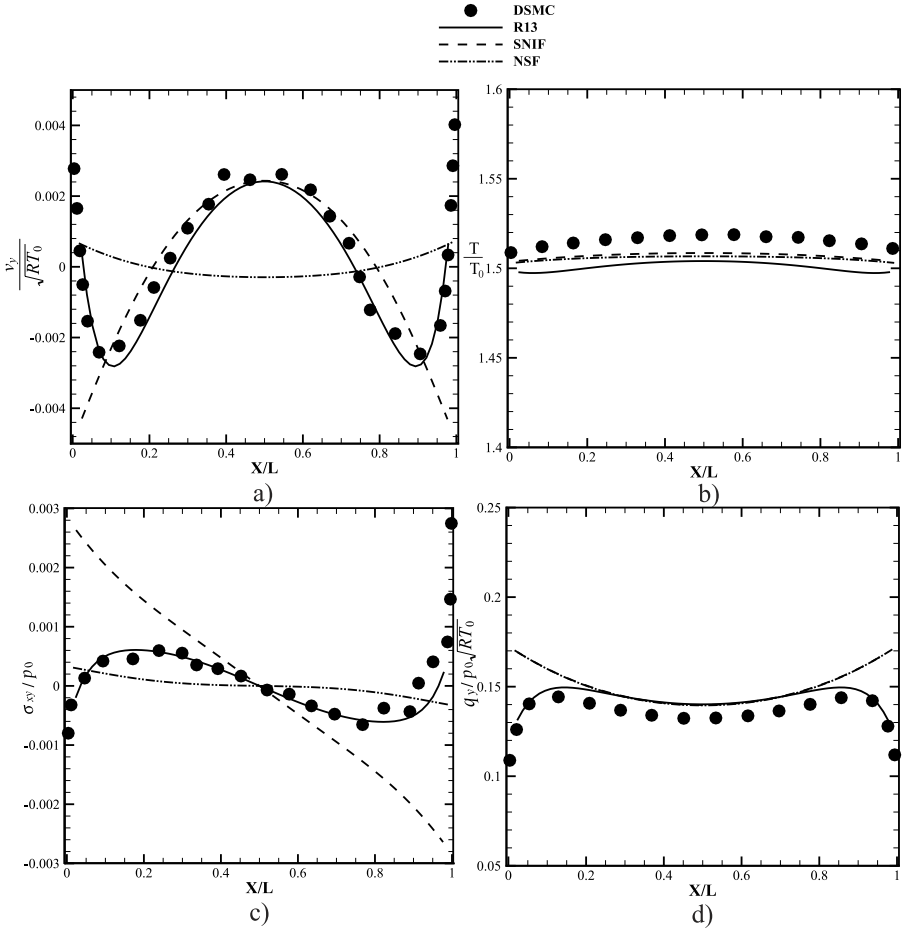

FIG. 6. Rarefied flow properties along horizontal centerline of the cavity with $\alpha = 0.2$, $\gamma = 0.9$, and $\Theta_0 = 1$ at $\mathrm{Kn}_0 = 0.04$. (a) Vertical velocity, (b) temperature, (c) shear stress, (d) vertical heat flux.

Note that thermal stress can also play a role at the boundary, and lead to so-called "thermal stress slip flow," in Ref. 14. However, in the current study, by accessing to different macroscopic methods, we can identify the source for each emerging vortices. Predicting the warm-to-cold vortex in the vicinity of the wall, by both NSF and R13 equations suggests that this vortex must be due to the (inverted) thermal transpiration effect.

For more insight into the capability of the different models, Fig. 6 shows the flow properties along the horizontal centerline of the cavity. DSMC, R13, and SNIF have a good agreement to DSMC for the vertical velocity v_y in the bulk of the gas. Considering that thermal stress is included in the SNIF but not the NSF equations, the deviation of the NSF results from the DSMC data shows the main role of the thermal stresses in this case. The deviation between SNIF and R13 results for the vertical velocity is large in the Knudsen layer, where the boundary effects dominate the flow behavior.

The temperature variation along the centerline is shown in Fig. 6(b). It is seen that the *relative* deviation of the three macroscopic models from the DSMC result is small, $\frac{T_{DSMC}-T_{R13}}{T_B-T_T} < 0.01$. This deviation can be attributed to the linearization of the boundary conditions, and rather large temperature ratio between the bottom and top walls.

The variation of the shear stress along the horizontal centerline is depicted in Fig. 6(c), where good agreement between DSMC and R13 results is evident. NSF and SNIF equations, however, show marked deviations, which are a further reflection of their inability to describe the flow field. The variation of vertical heat flux along the horizontal centerline is shown in Fig. 6(d). The effect of Knudsen layer that leads to reduction of the heat flux in the proximity of the surface is only captured by the R13 equations.

It is worth noting that the scale of velocity in Fig. 6 suggests that modeling this flow with DSMC is extremely difficult, and time consuming. For the sake of comparison with macroscopic methods

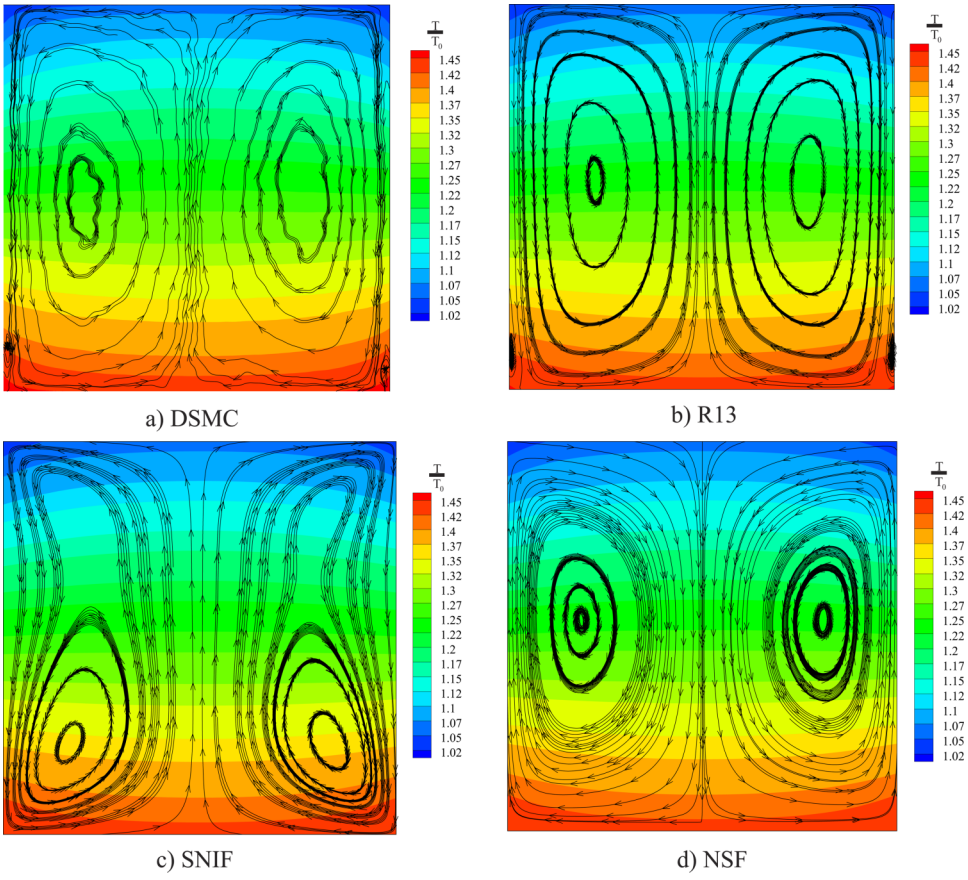

FIG. 7. Velocity streamlines overlaid on the temperature distribution for the VDM boundary conditions when $\frac{T_B}{T_T} = 1.5$, $\alpha = 0.2$, $\gamma = 0.9$, and $\Theta_0 = 1$ at $\mathrm{Kn}_0 = 0.02$.

(specially NSF), we were restricted on the magnitude of Knudsen number. Moreover, increasing the temperature ratio $\frac{T_B}{T_T}$ to more than 2 is not recommended for the macroscopic methods, due to the employed linearization in deriving R13 equations and boundary conditions. The resulting *small* velocity from considered temperature ratio leads to appearance of statistical noises in our DSMC results. By performing a statistical error study, we found that the noise to signal ratio for the *raw* DSMC results of Fig. 5(a) is approximately 10%. Also, we used a macroscopic filtering post-processor, as explained in Ref. 29, to extract the macroscopic moments from the raw DSMC results. This will reduce the remaining noises in the DSMC solution to some degrees and gives rather acceptable results. This problem is a good example for the importance of employing accurate macroscopic equations for modeling low speed microflows.

2. Thermal stress flow

Next, we consider the case where thermal stress (almost) takes over the entire flow field and drives the rarefied flow. For this means, we decrease the Knudsen number to $Kn = 0.02$, and the temperature ratio to $\frac{T_B}{T_T} = 1.5$, while keeping the same coefficients in the VDM boundary condition as before. The velocity streamlines overlaid on temperature distributions are depicted in Fig. 7. In here, the width of Knudsen layer, where the (inverted) transpiration force tries to move the flow from warm-to-cold becomes smaller. Similar to the previous case, neither the NSF nor the SNIF equations can resolve the interplay between the two thermal forces, and they both fail to predict the flow pattern.

The R13 and DSMC methods, however, predict two dominant thermal stress vortices in the bulk, as well as two small transpiration vortices in the vicinity of bottom corners. The smaller thermal

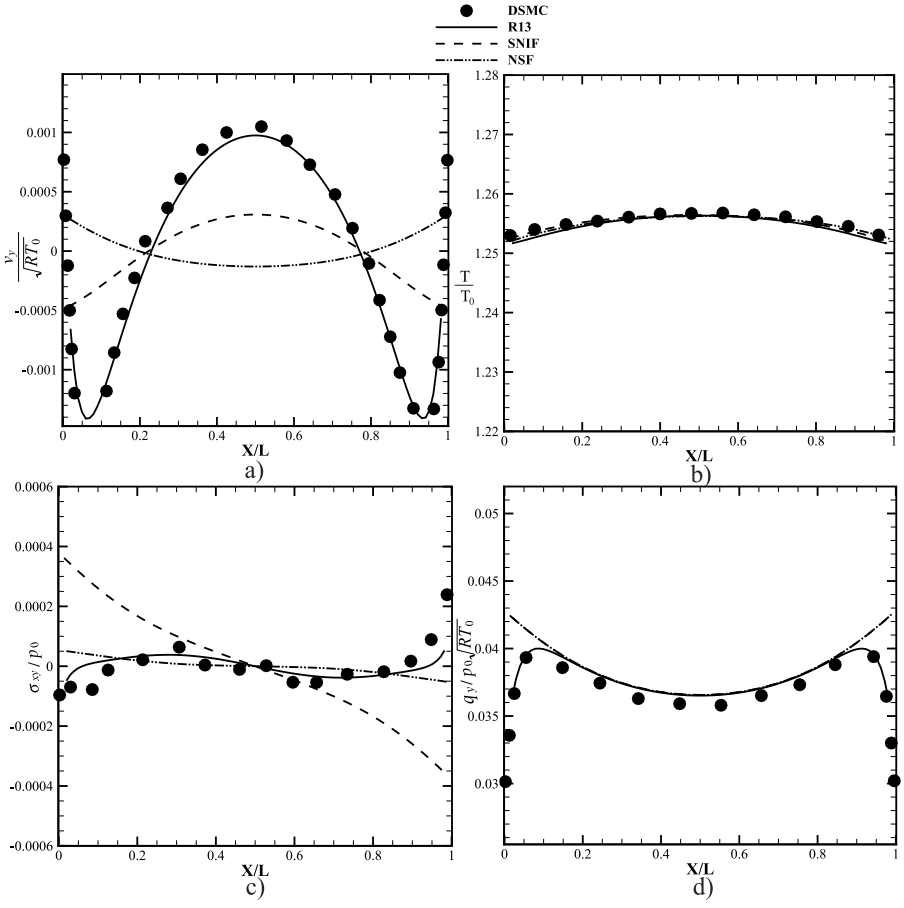

FIG. 8. Rarefied flow properties along horizontal centerline of the cavity when $\frac{T_B}{T_T} = 1.5$, $\alpha = 0.2$, $\gamma = 0.9$, and $\Theta_0 = 1$ at $\mathrm{Kn}_0 = 0.02$. (a) Vertical velocity, (b) temperature, (c) shear stress, (d) vertical heat flux.

gradient on the wall as well as smaller width of Knudsen layer pushes the transpiration vortices to the vicinity of bottom corners.

The flow properties along the horizontal centerline of the cavity is shown in Fig. 8. Due to the smaller temperature ratio in this case, the linearization technique employed in R13 equations remains more accurate, and the results have better agreement with the DSMC solution. Note that by decreasing the Knudsen number and temperature ratio, we weaken the driving forces in the thermal cavity. This is observed in the smaller magnitude of the velocity in Fig. 8(a). As a result, we can see that the temperature, shear stress, and heat flux profiles become more flat and approach to the case of thermal cavity with pure conduction.

V. CONCLUSION

Thermally driven flows are driven by the thermal transpiration force at the boundary, and the thermal stresses in the bulk. The Maxwell boundary model with velocity dependent accommodation coefficient allows to change the size and direction of the thermal transpiration force, which leads to marked changes in the balance of transpiration force and thermal stresses. The simulation of the thermally driven cavity shows that macroscopic methods are extremely useful tools for the interpretation of rarefied flows.

The transpiration force can be introduced into the jump and slip boundary conditions for classical hydrodynamics (NSF equations). However, since the NSF equations do not describe thermal stresses at all, they fail in the description of flows which are dominated by thermal stresses, and their interplay with a transpiration force. The equations for SNIF add the description of thermal stresses to classical hydrodynamics, and hence fare somewhat better. However, they fail for the flow considered here, since they can only describe the behavior in the bulk, but cannot resolve the flow field in the Knudsen layer in front of the wall. The R13 equations account for a larger number of rarefaction effects and give a good approximation to the flow even in the Knudsen layer; hence, they can provide a reasonably accurate description of all aspects of the flow.

While the DSMC method and other microscopic methods to solve the Boltzmann equation are highly accurate, they consume large numerical resources and time, and they cannot provide clear interpretations of the results. Macroscopic methods generally can only provide approximations to the exact microscopic solutions, but they are much cheaper, and faster, to solve. Moreover, since the equations relate macroscopic quantities with clear meaning, macroscopic models are rather helpful for the interpretation of flows. The presented simulations indicate that it is best to use macroscopic models that can (reasonably) capture all rarefaction effects, e.g., the R13 equations, rather than models that describe only selected effects.

ACKNOWLEDGMENTS

This research was supported by the Natural Sciences and Engineering Research Council (NSERC).

[1] C. Cercignani, *Theory and Application of the Boltzmann Equation* (Scottish Academic Press, Edinburgh, 1975).
[2] S. Chapman and T. G. Cowling, *The Mathematical Theory of Nonuniform Gases* (Cambridge University Press, 1970).
[3] Y. Sone, *Kinetic Theory and Fluid Dynamics* (Birkhauser, Boston, 2002).
[4] G. A. Bird, *Molecular Gas Dynamics and the Direct Simulation of Gas Flows* (Oxford University Press, Oxford, 1994).
[5] H. Struchtrup, *Macroscopic Transport Equations for Rarefied Gas Flows* (Springer, Berlin, 2005).
[6] M. N. Kogan, V. S. Galkin, and O. G. Fridlender, "Stresses produced in gases by temperature and concentration inhomogeneities. New types of free convection," Sov. Phys. Usp. **19**, 420–428 (1976).
[7] A. V. Bobylev, "Quasistationary hydrodynamics for the Boltzmann equation," J. Stat. Phys. **80**, 1063–1083 (1995).
[8] E. Yariv, "Thermophoresis due to strong temperature gradients," SIAM J. Appl. Math. **69**, 453–472 (2008).
[9] A. S. Rana, M. Torrilhon, and H. Struchtrup, "A robust numerical method for the R13 equations of rarefied gas dynamics: Application to lid driven cavity," J. Comput. Phys. **236**, 169 (2013).
[10] F. Sharipov and V. Seleznev, "Data on internal rarefied gas flows," J. Phys. Chem. Ref. Data **27**, 657–706 (1998).
[11] S. Kosuge, K. Aoki, S. Takata, R. Hattori, and D. Sakai, "Steady flows of a highly rarefied gas induced by nonuniform wall temperature," Phys. Fluids **23**, 030603 (2011).
[12] A. S. Rana, A. Mohammadzadeh, and H. Struchtrup, "A numerical study of the heat transfer through a rarefied gas confined in a micro cavity," Continuum Mech. Thermodyn. **27**, 433–446 (2014).

[13] K. Aoki, P. Degond, L. Mieussens, S. Takata, and H. Yoshida, "A diffusion model for rarefied flows in curved channels," SIAM Multiscale Model. Simul. **6**(4), 1281–1316 (2008).
[14] Y. Sone, "Flows induced by temperature fields in a rarefied gas and their ghost effect on the behavior of a gas in the continuum limit," Annu. Rev. Fluid Mech. **32**, 779–811 (2000).
[15] Y. Sone and T. Doi, "Ghost effect of infinitesimal curvature in the plane Couette flow of a gas in the continuum limit," Phys. Fluids **16**, 952–971 (2004).
[16] K. Aoki, Y. Sone, and Y. Waniguchi, "A rarefied gas flow induced by a temperature field: Numerical analysis of the flow between two coaxial elliptic cylinders with different uniform temperatures," Comput. Math. Appl. **35**, 15–28 (1998).
[17] H. Struchtrup, "Maxwell boundary condition and velocity dependent accommodation coefficient," Phys. Fluids **25**, 112001 (2013).
[18] W. Wagner, "A convergence proof for Bird's direct simulation Monte Carlo method for the Boltzmann equation," J. Stat. Phys. **66**, 1011 (1992).
[19] N. Hadjiconstantinou, A. Garcia, M. Bazant, and G. He, "Statistical error in particle simulations of hydrodynamic phenomena," J. Comput. Phys. **187**, 274–297 (2003).
[20] H. Struchtrup, "Scaling and expansion of moment equations in kinetic theory," J. Stat. Phys. **125**, 565–587 (2006).
[21] H. Struchtrup and M. Torrilhon, "Regularization of Grad's 13 moment equations: Derivation and linear analysis," Phys. Fluids **15**, 2668 (2003).
[22] H. Struchtrup and M. Torrilhon, "Higher-order effects in rarefied channel flows," Phys. Rev. E **78**, 046301 (2008).
[23] H. Struchtrup and M. Torrilhon, "Regularized 13 moment equations for hard sphere molecules: Linear bulk equations," Phys. Fluids **25**, 052001 (2013).
[24] H. Struchtrup and M. Torrilhon, "Boundary conditions for regularized 13-moment-equations for micro-channel-flows," J. Comput. Phys. **227**, 1982 (2008).
[25] J. C. Maxwell, "On stresses in rarefied gases arising from inequalities of temperature," Philos. Trans. R. Soc. London **170**, 231–256 (1879).
[26] C. Cercignani and M. Lampis, "Kinetic models for gas–surface interactions," Transp. Theory Stat. Phys. **1**, 101–114 (1971).
[27] R. G. Lord, "Some extensions to the Cercignani–Lampis gas–surface scattering kernel," Phys. Fluids A **3**, 706–710 (1991).
[28] F. Sharipov, "Application of the Cercignani–Lampis scattering kernel to calculations of rarefied gas flows. II. Slip and jump coefficients," Eur. J. Mech., B: Fluids **22**, 133–143 (2003).
[29] A. Mohammadzadeh and H. Struchtrup, "Velocity dependent Maxwell boundary conditions in DSMC," Int. J. Heat Mass Transfer **87**, 151–160 (2015).
[30] M. Epstein, "Predicting continuum breakdown of rarefied micro/nano flows using entropy and entropy generation analysis," AIAA J. **5**, 1797 (1967).
[31] H. Struchtrup and P. Taheri, "Macroscopic transport models for rarefied gas flows: A brief review," IMA J. Appl. Math. **76**, 672 (2011).
[32] H. Grad, "On the kinetic theory of rarefied gases," Commun. Pure Appl. Math. **2**, 331 (1949).